SCFN: A Deep Network for Functional Urban Impervious Surface Mapping Using *C*-Band and *L*-Band Polarimetric SAR Data

Jing Ling, *Graduate Student Member, IEEE*, Hongsheng Zhang, *Senior Member, IEEE*, Rui Liu, *Graduate Student Member, IEEE*, and Yinyi Lin, *Member, IEEE*

***Abstract*—Accurate and timely monitoring of functional urban impervious surfaces (FUISs), such as ports, roads, and buildings, is essential yet challenging for complex coastal cities due to their cloudy weather and diverse land surfaces. Synthetic aperture radar (SAR) provides unique all-weather observation capabilities for prompt and regular urban mapping. However, SAR scattering information is limited to distinguish impervious surfaces with similar scattering responses but different functions. This study develops a scattering–compactness fusion network (SCFN), which integrates SAR polarimetric scattering and object compactness characteristics for enhanced FUIS recognition. Central to our approach is the scattering object compactness index, which is specifically designed to capture the distinct spatial patterns and compactness of scattering objects and complement their intrinsic scattering signatures. The dual-branch SCFN concurrently extracts and fuses object-scale scattering and compactness features using tailored network architectures. Experiments on *L*-band and *C*-band fully polarimetric ALOS-2 and GF-3 data in Hong Kong, as well as *L*-band dual-polarized ALOS-2 data, are undertaken to verify SCFN's effectiveness, achieving up to 8% improvement in the overall FUIS classification accuracy over baselines. The transferability of SCFN is further validated using fully polarimetric ALOS-2 data in Shenzhen, where consistent performance improvements are observed. The successful application of SCFN in both coastal cities highlights the potential of joint scattering–compactness modeling for advanced SAR-based urban mapping and its robustness across different urban landscapes.**

***Index Terms*—Impervious surface, scattering, scattering–compactness fusion network (SCFN), synthetic aperture radar (SAR), urban function.**

Manuscript received 31 January 2024; revised 19 March 2024, 14 May 2024, and 20 June 2024; accepted 2 July 2024. Date of publication 15 July 2024; date of current version 5 August 2024. This work was supported in part by the Research Grants Council (RGC) of Hong Kong, China, under Grant HKU27602020, Grant HKU17613022, and Grant HKU14605917, in part by the National Natural Science Foundation of China under Grant 42022061 and Grant 42071390, in part by Shenzhen Science and Technology Program under Grant JCYJ20210324124013037, and in part by the Seed Funding for Strategic Interdisciplinary Research Scheme of The University of Hong Kong. *(Corresponding author: Hongsheng Zhang.)*

The authors are with the Department of Geography, The University of Hong Kong, Hong Kong, China, and also with the University of Hong Kong Shenzhen Institute of Research and Innovation, Shenzhen 518057, China (e-mail: jingling@connect.hku.hk; zhanghs@hku.hk; rhysliu@connect.hku.hk; yinyilin@hku.hk).

Digital Object Identifier 10.1109/JSTARS.2024.3427839

I. Introduction

CITIES are major hubs of human activity and play a crucial role in studying global social, economic, and environmental trends. With over half of the world's population concentrated in urban areas, understanding cities is key to tackling issues, such as poverty, sustainability, and quality of life. Coastal cities, particularly those with high density and urbanization levels, require close study as they connect inland areas to maritime trade and have undergone explosive growth in recent decades [1]. Rapid development of transportation, tourism, port facilities, and housing in coastal cities also impacts fragile coastal ecosystems [2].

Monitoring the distribution of functional urban impervious surfaces (FUISs), such as roads, buildings, and ports, is vital for coastal city research. FUIS differentiates between impervious surfaces that support various urban functions, such as roads, buildings, and port operations, thereby providing more detailed information on impervious surfaces in urban environments. FUIS mapping allows us to quantify urban expansion, analyze economic development patterns, and identify threats to natural habitats [3]. Detailed FUIS data facilitate urban planning and growth management to balance economic prosperity with residents' well-being and environmental protection. FUIS extent also indicates the potential for flooding, urban heat islands, and other hazards amplified by impervious surfaces. Therefore, accurate and up-to-date FUIS mapping in dynamic coastal settings is essential. Although optical data enable reliable UIS identification in cloud-free scenarios, the performance degrades under cloud cover due to obstruction of surface information. Studies have shown that optical images struggle with accurate urban classification in cloudy regions [4]. In contrast, synthetic aperture radar (SAR) imagery provides all-weather, day-and-night imaging capabilities unaffected by cloud cover.

Polarimetric SAR (PolSAR) satellites operating at different wavelengths exhibit distinct scattering characteristics when interacting with the Earth's surface. *L*-band SAR, with its longer wavelength, demonstrates superior penetration capabilities compared with shorter wavelengths, such as *C*-band and *X*-band [5], [6], which allows *L*-band SAR to effectively capture information from beneath vegetation canopies and penetrate through building structures, while *C*-band and *X*-band SAR are more sensitive to surface roughness and primarily capture scattering information from the top of the canopy. Polarization also plays

© 2024 The Authors. This work is licensed under a Creative Commons Attribution-NonCommercial-NoDerivatives 4.0 License. For more information, see https://creativecommons.org/licenses/by-nc-nd/4.0/

a crucial role in SAR data interpretation. Different polarization configurations, such as dual polarization and fully polarimetric data, provide varying levels of information about the scattering properties of the Earth's surface [7].

PolSAR has shown promise for various applications [8], [9]. Polarimetric scattering features describe the scattering mechanisms of the target. To analyze and interpret PolSAR imagery, incoherent target decomposition methods are commonly employed to derive these scattering characteristics [10]. These methods are categorized into eigenvalue-based decompositions [11], [12] and model-based decomposition [13], [14]. The eigenvalue-based decomposition techniques utilize the eigenvalues and eigenvectors of either the coherency or covariance matrix to elucidate the scattering mechanisms. Among these, the Cloude decomposition method is particularly notable [11], which utilizes four independent polarization parameters that define the polarization space, along with scattering entropy and anisotropy, to interpret PolSAR images. On the other hand, the Freeman–Durden three-component decomposition is a well-known model-based approach [13], which investigates scattering characteristics using scattering models with clear physical meaning. Another powerful tool for interpreting PolSAR images is polarimetric signatures [15]. By varying the polarization basis, these methods extract detailed scattering characteristics and visualize them in a 3-D plane [16]. This approach provides a comprehensive understanding of the geometrical and physical properties of targets [17]. Numerous studies have focused on land surface mapping using various PolSAR features, including Freeman, Yamaguchi, Cloude–Pottier, and H/A/alpha decompositions [18], [19]. Different classification methods were employed to conduct the land surface classification, such as the maximum likelihood-based methods, support vector machines, and random forests [20], [21].

Despite recent advances in PolSAR technology, compared with the rich spectral information from optical imagery, SAR scattering mechanics are more complex and the scattering signatures of different land cover types are not yet fully understood [22], [23]. While impervious surface classification using PolSAR has been extensively studied at the pixel level using features, such as scattering matrix parameters and polarimetric features [23], [24], [25], research at the object level has gained some attention by exploiting PolSARs advantages in speckle suppression and information preservation. Wang et al. [26] utilized object-based image classification of multitemporal SAR images to map permafrost landscape features. Habibi et al. [27] performed a classification of PolSAR data based on object-based multiple classifiers for urban land cover. Liu et al. [28] integrated convolutional neural networks and object-based postclassification refinement for land use and land cover mapping. Unlike pixel-based methods, which classify each pixel individually, object-oriented approaches first segment the image into objects representing meaningful real-world features. This helps reduce local speckle noise while preserving shape information. Object-level features can then be extracted to better characterize different land cover classes. However, object-oriented approaches segment objects without clarifying what scattering characteristics distinguish the FUIS objects in PolSAR, unlike in optical imagery where different surface objects often have distinct spectral signatures [29]. This is attributed to the rich spectral data from optical sensors that enable the differentiation of various land covers based on their distinct spectral response patterns. But in PolSAR, the scattering mechanisms of different surfaces are complex and variable, as SAR scattering is sensitive to surface properties, such as geometry, roughness, and dielectric constant [30]. Further investigation on the scattering mechanisms of different surfaces and the scattering characteristics that determine the division of objects is required.

Moreover, detailed FUIS mapping poses greater recognition challenges but has received little focus [31]. This is challenging since SAR provides limited scattering information while different FUIS types can have similar backscatter signatures. Therefore, apart from the scattering characteristics of the land surfaces, other potential information that might help distinguish the FUIS types from nonimpervious surfaces (NISs) warrants further study. Spatial features are widely used in optical imagery for classification improvement [32], [33], but their efficacy in SARs distinct imaging modality is unclear due to its distinct imaging mechanics compared with optical modalities. How to measure the spatial characteristics of objects in scattering images and whether object spatial information contains discriminative information in distinguishing between FUIS and NISs in SAR imagery requires further study.

This study focuses on the identification of FUIS in high-density coastal urban environments using SAR data under different scenarios. These cities often experience complex land surface changes due to factors, such as fast-paced urbanization, intricate urban planning, and diverse land use patterns. The high concentration of population and infrastructure in these areas necessitates detailed and accurate FUIS information for effective urban management and planning. Moreover, the coastal location of these cities, often characterized by humid climates and frequent cloud cover, emphasizes the need for alternative data sources, such as SAR, that can penetrate through clouds and provide reliable data for monitoring urban impervious surfaces. The complexity of urban microwave scattering mechanisms and the scattering differences among SAR data with different wavelengths and polarizations add to the challenges of FUIS identification. This study also aims to investigate the scattering characteristics of urban impervious surfaces under different SAR configurations and develop robust and adaptable methods for accurate FUIS mapping applicable to various SAR datasets. Considering the aforementioned issues of limited SAR scattering information and unclear mechanisms of scattering spatial information for FUIS objects, this study makes the following three contributions through in-depth PolSAR scattering analysis: First, we propose a scattering object compactness index (SOCI) that characterizes the compactness properties of different FUIS and NIS objects on scattering feature images. The SOCI provides supplementary information to SAR backscatter for distinguishing between FUIS and NIS objects. Second, we develop a scattering–compactness fusion network (SCFN) to integrate scattering and compactness clues for FUIS recognition.

The SCFN is innovatively designed to fit the UIS scattering object patch and support deep convolution and fusion for compactness and scattering features. Third, different from existing pixel-based networks, the SCFN operates on FUIS-level object patches as input and is designed to effectively extract object spatial contextual details for FUIS characterization. To validate the effectiveness and robustness of the proposed methods, we conducted extensive experiments using *L*-band and *C*-band fully polarimetric ALOS-2 and GF-3 data, and dual-polarization SAR data in two representative coastal cities, Hong Kong (HK) and Shenzhen. The diverse datasets and urban environments allowed us to comprehensively assess the performance and transferability of the SCFN approach. This research provides new insights into SAR-based urban mapping by developing an interpretable SOCI and an advanced object-oriented deep model. The integration of scattering and compactness information in a tailored network structure overcomes the limitations of previous approaches and contributes to expanding the capabilities of SAR systems for all-weather FUIS mapping. The frameworks established could be extended to other PolSAR urban applications.

II. Study Area and Dataset

This study focuses on two major coastal cities in southern China: HK and Shenzhen. Both cities are situated in the Pearl River Delta region and are known for their rapid urbanization, high population density, and significant roles in international trade and finance.

HK is one of the world's most densely populated cities with over 7 million residents crammed into just 1100 km^2 of land area. As a major Asian financial center and global transportation hub, HK plays a pivotal role in international trade and finance. The Kwai Chung Port of HK is strategically located on the far east trade routes and is the geographical center of the now fast-developing Aisa–Pacific Basin. Its uninterrupted operation, especially during global crises, such as the COVID-19 pandemic, is, thus, of great socioeconomic importance. Shenzhen is another thriving metropolis in the Pearl River Delta. It has experienced phenomenal growth since its designation as China's first special economic zone in 1980, transforming from a small fishing village to a global technology and innovation hub. With a population of over 17 million and a land area of 1997 km^2, Shenzhen is also one of the most densely populated cities in China. Shenzhen's rapid urbanization has led to the expansion of impervious surfaces, including dense residential buildings and extensive road networks.

Both HK and Shenzhen's extensive functional impervious surfaces, such as ports, buildings, roads, and railways, are central to its position as a thriving international metropolis and regional economic hub. Timely monitoring and management of critical FUIS infrastructure is, thus, essential for maintaining operational flows and managing the urbanization process in these cities. However, frequent heavy rain and persistent cloud cover pose a major obstacle, often obstructing optical satellite monitoring during critical periods as satellite optical sensors are unable to penetrate thick clouds.

In contrast, SAR provides all-weather day-and-night imaging capabilities unaffected by clouds or rain. SAR has shown high potential for frequent monitoring of HKs FUIS, including ports, buildings, roads, and railways, overcoming limitations of optical data [22]. SARs unique sensitivity to surface properties, such as structure, material, and moisture, further aids the classification and mapping of different impervious surface types. Therefore, HK and Shenzhen's cloudy climate, the economic importance, and SARs all-weather imaging advantages make them ideal study sites for investigating SAR-based FUIS mapping, which can provide timely and reliable information for urban management. The methods developed in this challenging environment could also be applied to other coastal cities with similar climate conditions and FUIS mapping needs. An illustrative map of the geographic location and the optical and SAR images of the study areas are shown in Fig. 1.

Three sets of fully PolSAR data were utilized in this research: two *L*-band ALOS-2 PALSAR-2 fully polarimetric scenes with a 5-m resolution, covering HK and Shenzhen, respectively, and one *C*-band Gaofen-3 (GF-3) fully polarimetric scene with an 8-m resolution, covering HK. Both ALOS-2 and GF-3 were obtained in quad-polarization mode, which transmits and receives signals in two orthogonal polarizations—vertical (V) and horizontal (H)—measuring the complete scattering matrix with all four combinations (HH, HV, VH, and VV). In addition to the fully polarimetric data, the feasibility of using dual-polarization data for FUIS classification was explored. For this purpose, we extracted the dual-polarization (HH and HV) data from the ALOS-2 data of HK. The dual-polarization data offer a reduced set of polarimetric information compared with the fully polarimetric data. The inclusion of both HK and Shenzhen study areas, as well as the utilization of data from different SAR sensors (ALOS-2 and GF-3) and polarization settings (fully polarimetric and dual polarization), enables a robust evaluation of the transferability and adaptability of the proposed method under diverse data conditions and urban landscapes. The SAR datasets underwent preprocessing, including radiometric calibration, speckle noise filter, and polarimetric decomposition. The processed data were then geocoded into WGS84 UTM 49N projection using a digital elevation model for terrain correction. In addition, WorldView-2 multispectral optical images with 1.6-m resolution were used as reference for visual interpretation and manual annotation of the SAR data. Unlike optical data, SAR imagery has distinct imaging mechanics and scattering characteristics that make visual analysis challenging. The fine details discernible in the high-resolution optical image aided the accurate ground truth labeling of different functional impervious surfaces for algorithm training and evaluation.

III. Methodology

Based on the scattering characteristics of the land surfaces, this study first proposes a UIS SOCI, which measures the specific shape compactness of artificial and natural land covers in PolSAR scattering. We then develop an SCFN to integrate the scattering and object compactness information for FUIS recognition.

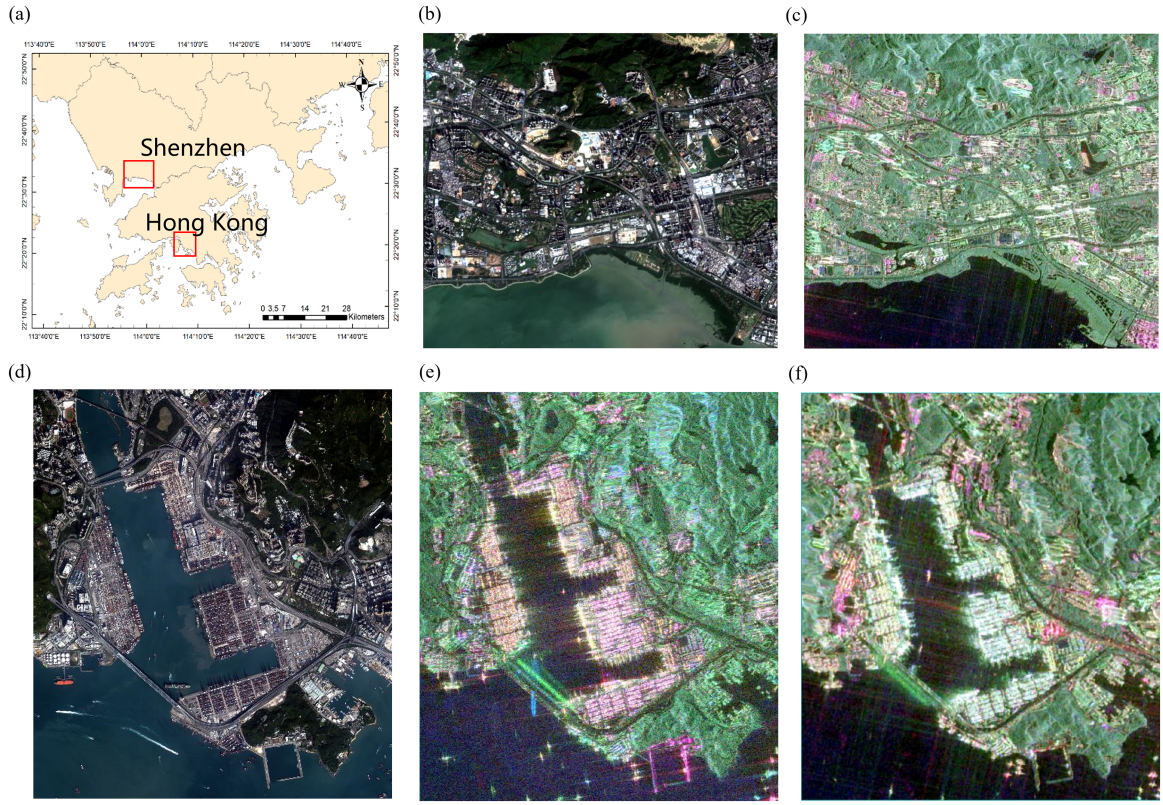

Fig. 1. (a) Geographic location, (b) optical image, and (c) ALOS-2 image of Shenzhen, and (d) optical image, (e) ALOS-2 image, and (f) GF-3 image of HK.

A. PolSAR Scattering

PolSAR data contain abundant scattering information through the polarimetric scattering matrix [*S*], which characterizes the complex electromagnetic interactions

$$[S] = \begin{bmatrix} S_{HH} & S_{HV} \\ S_{VH} & S_{VV} \end{bmatrix} \tag{1}$$

where S_{XY} denotes the scattering coefficient for *X*-polarization transmission and *Y*-polarization reception. Based on the reciprocal assumption between cross polarizations, the coherence matrix *T* containing full polarimetric information can be derived (2) shown at the bottom of this page, where $\boldsymbol{T}_{ij}$ is the (*i,j*)th element. Diagonals $\boldsymbol{T}_{11}$, $\boldsymbol{T}_{22}$, and $\boldsymbol{T}_{33}$ represent the surface, double-bounce, and volume scattering, respectively.

Multiple PolSAR features were extracted, including $\boldsymbol{T}_{11}$, $\boldsymbol{T}_{22}$, $\boldsymbol{T}_{33}$, and backscatter coefficients (HH, HV, VH, and VV) to fully characterize scattering properties. Polarimetric decomposition methods, including Freeman–Durden decomposition [13], Cloude–Pottier decomposition [11], H/A/α decomposition [34], and Yamaguchi four-component decomposition [14], were applied to further analyze scattering mechanisms of different land covers. These techniques have proven effective in previous PolSAR classification studies [24].

Fig. 2 shows false color composites of the derived PolSAR features from the ALOS-2 data in HK. In Fig. 2(b) and (c), Freeman and Yamaguchi features representing double-bounce, volume, and surface scattering are mapped to R, G, and B channels, respectively. Urban structures, such as buildings, appear red due to double bounce, while vegetation is green from volume scattering. Smooth surfaces, such as water, are blue because of surface scattering. Entropy, anisotropy, and alpha (R, G, and B channels, respectively) in the Cloude and H/A/α decomposition [see Fig. 2(a) and (d)] provide complementary scattering information. Entropy represents scattering randomness. Anisotropy describes the relative importance of the secondary scattering mechanisms. The alpha angle relates to the type of scattering mechanism. Surfaces, such as vegetation, have high entropy and appear red. Alpha indicates the dominant scattering type—high alpha corresponds to double-bounce scattering from dihedral structures, such as buildings, which appear blue. Backscattering coefficients in Fig. 2(e) show the intensities of HV, VV, and HH,

$$T = \begin{bmatrix} T_{11} & T_{12} & T_{13} \\ T_{21} & T_{22} & T_{23} \\ T_{31} & T_{32} & T_{33} \end{bmatrix} = \frac{1}{2} \begin{bmatrix} \left\langle |S_{\mathrm{HH}} + S_{\mathrm{VV}}|^2 \right\rangle & \langle (S_{\mathrm{HH}} + S_{\mathrm{VV}})(S_{\mathrm{HH}} - S_{\mathrm{VV}})^* \rangle & \langle 2(S_{\mathrm{HH}} + S_{\mathrm{VV}}) S_{\mathrm{HV}}^* \rangle \\ \langle (S_{\mathrm{HH}} - S_{\mathrm{VV}})(S_{\mathrm{HH}} + S_{\mathrm{VV}})^* \rangle & \left\langle |S_{\mathrm{HH}} - S_{\mathrm{VV}}|^2 \right\rangle & \langle 2(S_{\mathrm{HH}} - S_{\mathrm{VV}}) S_{\mathrm{HV}}^* \rangle \\ \langle 2S_{\mathrm{HV}}(S_{\mathrm{HH}} + S_{\mathrm{VV}})^* \rangle & \langle 2S_{\mathrm{HV}}(S_{\mathrm{HH}} - S_{\mathrm{VV}})^* \rangle & \left\langle 4|S_{\mathrm{HV}}|^2 \right\rangle \end{bmatrix} \tag{2}$$

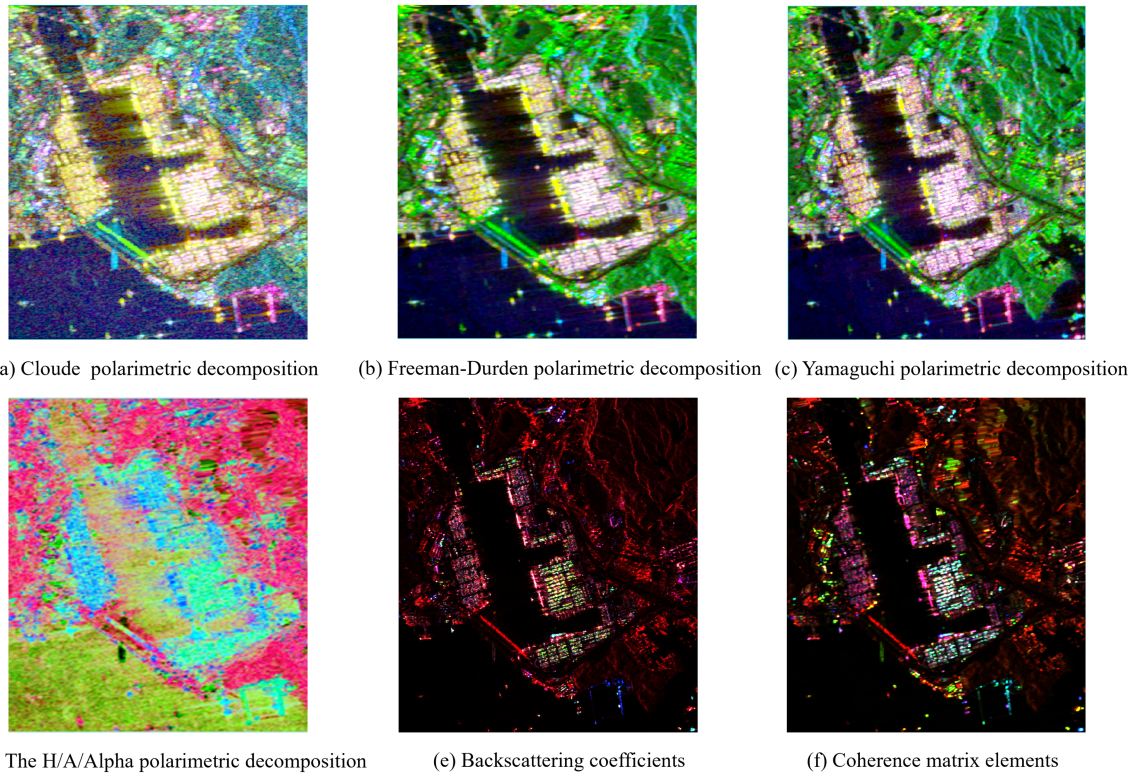

(a) Cloude polarimetric decomposition (b) Freeman-Durden polarimetric decomposition (c) Yamaguchi polarimetric decomposition

(d) The H/A/Alpha polarimetric decomposition (e) Backscattering coefficients (f) Coherence matrix elements

Fig. 2. PolSAR scattering features. (a) Cloude decomposition feature. (b) Freeman decomposition feature. (c) Yamaguchi decomposition feature. (d) H-A-Alpha decomposition feature. (e) Backscattering coefficient feature. (f) Coherence matrix feature from the ALOS-2 data in HK.

displayed in RGB channels, respectively. Smooth surfaces showing surface scattering with weak backscatter, such as calm water and smooth roads, appear dark. Rough surfaces, such as trees, have weaker HH and VV but stronger cross-polarizations HV and VH, thus appearing reddish. The scattering matrix diagonal in Fig. 2(f), (R, G, B: $\boldsymbol{T}_{33}, \boldsymbol{T}_{11}, \boldsymbol{T}_{22}$), related to volume scattering, surface scattering, and double-bounce scattering, respectively, provides similar complementary information.

In general, different features provide consistent but complementary scattering clues. Land covers, such as vegetation, water, and built-up areas, can be roughly identified. For detailed classification, combining multiple features helps distinguish different functional impervious surfaces based on their unique scattering signatures [10]. However, confusion exists between complex urban classes, motivating more advanced techniques to fully exploit PolSARs rich scattering information.

In general, there is an agreement between the different scattering features, but each provides complementary information. Different functional impervious surfaces demonstrate distinct scattering characteristics in the PolSAR imagery. Port areas appear bright across all feature images, owing to strong backscatter from their metallic structures and dielectric properties. Roads exhibit darker tones due to predominant surface scattering from their relatively smoother surfaces. Residential buildings with complex roof shapes produce more volume scattering, while nonresidential buildings favor double-bounce scattering. Therefore, the combination of multiple complementary PolSAR features aids the differentiation of detailed FUIS classes based on their scattering signatures. However, the mixing of scattering types is commonly observed in complex urban environments. Although PolSAR data enable coarse discrimination between impervious and NISs, uncertainties remain in finer level FUIS classification. Advanced techniques are required to fully exploit the rich scattering information for improved FUIS recognition.

B. Scattering Object Compactness Index

PolSAR features exhibit distinct scattering characteristics for certain functional impervious surfaces, aiding in their separation from other land covers. Buildings and other man-made structures favor double-bounce scattering. However, ports appear brighter due to the strong reflections from abundant metallic elements [22]. In contrast, the relatively smoother surfaces of roads primarily cause surface scattering, leading to weaker backscatter and showing darker tones [35]. Vegetation is dominated by volume scattering from its nonuniform canopy structures. Water bodies act as specular reflectors resulting in very low backscatter. Moreover, due to the high conductivity of water, radar signals can penetrate deep into the water body and be strongly attenuated and absorbed [36]. Therefore, the echo intensity of the water body might be weak. Soil demonstrates medium intensity surface or volume scattering depending on roughness and moisture content [37].

The distinct scattering signatures of different land cover types result in clear delineations between FUIS and NIS, such as vegetation and water in the SAR imagery. For instance, the strong double bounce and metallic reflections from man-made structures, such as buildings and ports, cause them to exhibit

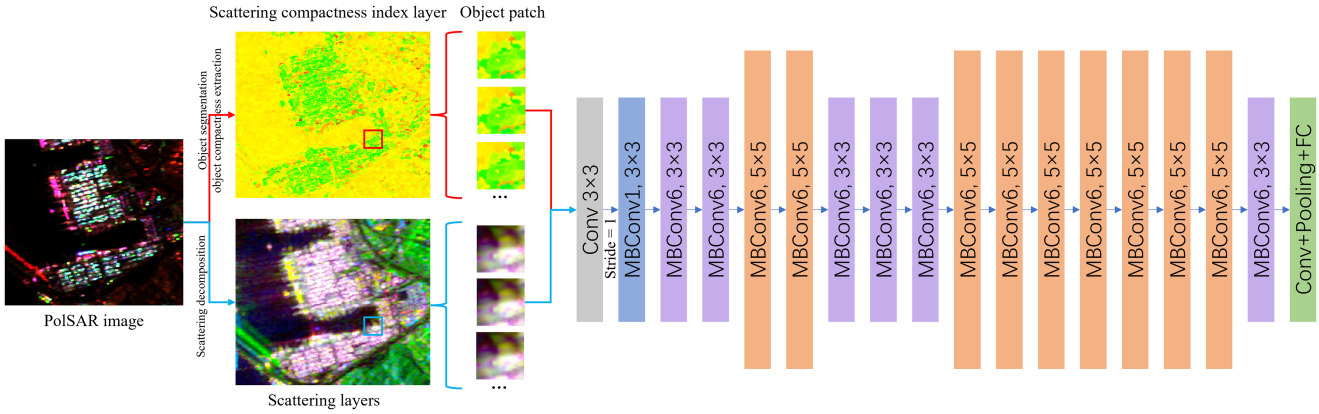

Fig. 3. Proposed SCFN architecture.

high radar double-bounce backscatter contrasts with surrounding low-scattering vegetation and water. Therefore, the different electromagnetic scattering behaviors of various urban land covers enable their scattering boundaries and, thus, can be segmented into distinct image objects. Moreover, owing to their artificial regular materials, FUIS objects usually show distinct scattering–compactness with more narrow and rectangular-related shapes. Different FUIS types also display unique compactness characteristics. For instance, long narrow roads can be distinguished from the regular rectangular shapes of ports and buildings. In contrast, homogeneous natural covers, such as water, might show more round shapes rather than narrow shapes.

Scattering information of individual samples is usually used to identify the land cover in PolSAR classification, where the spatial relationships and contextual connections of land covers are often ignored. Based on the above-mentioned analysis, this work introduces the spatial compactness of scattering to aid FUIS classification using scattering signatures. The image is first segmented into objects delineated by the combined PolSAR scattering contrasts between land covers by multiresolution segmentation [38]. Then, combining the scattering spatial compactness information, we propose an SOCI that measures the spatial compactness of image objects to complement the scattering features to better distinguish UIS and NIS samples with similar scattering behavior. The SOCI is shown as follows:

$$\mathrm{SOCI} = \frac{\sqrt{A_o}}{b_o} \tag{3}$$

where SOCI is the scattering object compactness index, A_o is the area of the scattering object, and b_o is the border length of the scattering object. An object with a more narrow and not compact shape (UIS) will have a lower compactness index value, while a compact object (circle or almost circle) (NIS) will have a higher SOCI value. The SOCI provides a new object compactness perspective to identify detailed UIS types from their scattering signatures.

C. Scattering–Compactness Fusion Network

To integrate the complementary scattering and object compactness characteristics for optimal FUIS identification, we develop an SCFN, as illustrated in Fig. 3.

EfficientNet is selected as the SCFN backbone for its state-of-the-art accuracy and efficiency over other CNN architectures [39]. Several innovative modifications are incorporated into SCFN tailored for FUIS classification based on the unique PolSAR scattering and compactness features.

First, to fit the spatial scale of urban land cover objects and provide essential contextual information, a 7×7 PolSAR patch centered on each pixel is extracted as input to SCFN. Unlike general natural image classification tasks, impervious surfaces in urban environments are typically smaller targets. Using large input sizes, such as 224×224, poses several challenges. First, it is difficult to obtain large homogeneous patches for these small targets. Second, severe overlap between adjacent image patches can degrade the model's performance. Previous research in remote sensing image classification has demonstrated the superiority of small patch sizes, such as 7×7, for detecting smaller objects [40], [41], [42], [43], [44], [45]. Considering these findings, a small 7×7 patch size is adopted in this study, as it provides sufficient neighborhood context while avoiding contamination from adjacent land cover types. Consequently, the model architecture is adapted to accommodate the chosen input patch size.

Second, pooling layers are typically utilized to reduce feature map dimensions for overfitting control in CNNs. However, for the small object patch input size, pooling leads to insufficient feature resolution for subsequent convolutional operations, restricting network depth. Therefore, considering the reduced input scale conforming to urban object size, convolutional and pooling layers as well as MBConv blocks are customized with stride 1 to maintain feature dimensions. This enables constructing a deeper network capable of extracting multiscale features despite the small input patches.

Third, given the complementary information provided by the scattering and compactness characteristics of land surfaces for differentiating both UIS versus NIS and detailed FUIS subclasses, the initial scattering layer and derived scattering–compactness index layer from the land surface patches are fused and then fed into subsequent deep networks in SCFN for extracting high-dimensional information and identifying FUIS categories.

The end-to-end training process enables adaptive learning of the scattering and compactness feature fusion and classification in a unified framework. By leveraging SARs distinctive

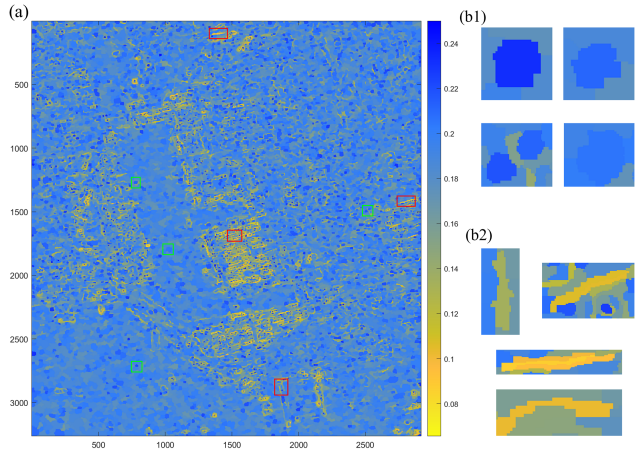

Fig. 4. (a) Whole SOCI features from the ALOS-2 data in HK, zoomed-in views of the (b1) green and (b2) red boxed regions in (a).

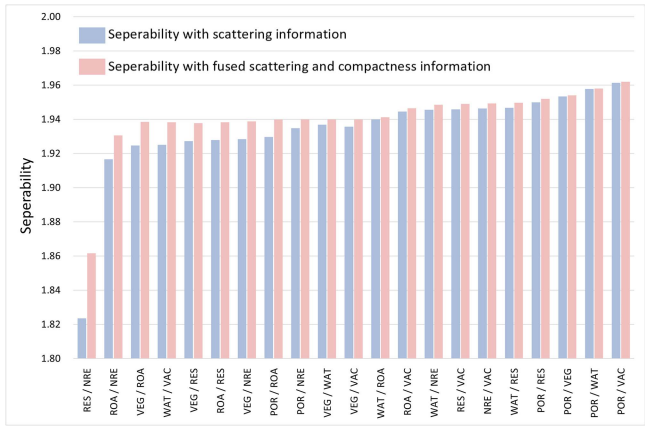

Fig. 5. Separability between different land covers using solely scattering features and jointly scattering and SOCI features from the ALOS-2 data in HK.

sensitivity to both scattering mechanisms and spatial structures, SCFN can effectively identify detailed FUIS categories from complex urban environments. Implemented in PyTorch 1.10.2, SCFN adopts EfficientNet-B0 as the backbone architecture. Key training hyperparameters include a batch size of 128, 50 iteration epochs, and an initial learning rate of 0.0001.

Experimental samples of different land cover types are carefully collected with the aid of high-resolution optical imagery and field surveys. The labeled samples are split into balanced training and testing sets with a 1:1 ratio. Functional impervious surface subclasses include port (POR), road (ROA), residential building (RES), and nonresidential building (NRE) defined based on urban planning criteria. NIS types comprise vegetation (VEG), vacant (VAC), and water (WAT).

IV. Experiments and Results

A. Evaluation of Object Compactness Information

The derived SOCI from the ALOS-2 data in HK provides intuitive visualization and quantification of compactness patterns for different land cover types (see Fig. 4). In the SOCI map, lower values are displayed in yellow indicating more narrow and not compact shape, while higher values in blue denote more compact shape (circle or almost circle).

Fig. 4(a) shows the whole SOCI results. To better visualize the compactness patterns, Fig. 4(b1) and (b2) provides zoomed-in views of the green and red boxed regions in Fig. 4(a), respectively. NISs, such as vegetation and water, in the green box of Fig. 4(b1) exhibit notably higher SOCI values portrayed in blue, corresponding to their concentrated and rounded scattering shape. In contrast, UISs, such as roads and buildings, in the red box of Fig. 4(b2) possess lower SOCI characterized by yellow colors, owing to their elongated and regular scattering patterns. The zoomed examples demonstrate how the SOCI complements scattering signatures by quantifying spatial context and compactness differences between land surface types. This complements the polarization scattering signatures by quantifying the spatial compactness distinctions between urban land surface types.

To validate the ability of SOCI to discriminate challenging surface classes, we further evaluated the separability between different land covers using solely scattering features and jointly using scattering and SOCI features from the ALOS-2 data in HK. The results are presented in Fig. 5 using the Jeffries–Matusita distance, a widely applied separability measure [46]. It can be observed that combining compactness information improves the separability for all land cover pairs to varying degrees. In particular, residential (RES) and nonresidential (NRE) buildings exhibit the lowest separability with scattering features alone, as both share similar urban constructions. However, fusing spatial cues significantly enhances their distinction, demonstrating the value of spatial context and compactness for differentiating these confused FUIS subclasses. Furthermore, compactness provides noticeable benefits in separating other impervious pairs, such as roads (ROA) versus nonresidential (NRE), as well as impervious versus nonimpervious classes, such as vegetation (VEG) versus roads. In contrast, ports (POR) are already well separated from other nonimpervious classes, owing to their distinct metallic scattering properties; thus, the enhancement from compactness is more marginal.

In summary, the quantitative separability analysis highlights that complementing polarimetric scattering with scattering–compactness information leads to improved delineation of both FUIS subtypes and between impervious and nonimpervious land covers. This validates the capability of SOCI for characterizing scattering spatial patterns to aid SAR classification.

B. Quantitative Assessment of Classification Accuracy

To validate the effectiveness of the proposed model, experiments were conducted on several datasets: fully polarimetric ALOS-2, fully polarimetric GF-3, and dual-polarized ALOS-2 data in HK. The Shenzhen area was additionally included in this study to further validate the effectiveness and transferability of the proposed SCFN method. Due to the difficulty and extensive effort required for fully polarimetric data acquisition and labeling, the experiments in Shenzhen were carried out using the *L*-band fully polarimetric ALOS-2 data.

TABLE I
COMPARISON OF THE OA, THE PA, AND THE UA OF SCON AND SCFN ON FULLY POLARIMETRIC ALOS-2, FULLY POLARIMETRIC GF-3, AND DUAL-POLARIZED ALOS-2 DATA IN HK AND SHENZHEN

		SCON				SCFN			
		HK_ALOS-2	HK_GF-3	HK_Dual_ALOS-2	SZ_ALOS-2	HK_ALOS-2	HK_GF-3	HK_Dual_ALOS-2	SZ_ALOS-2
PA(%)	NRE	55.66	53.12	32.47	57.39	57.79	57.28	34.13	63.23
	POR	84.54	72.72	58.61	/	86.35	78.53	63.44	/
	ROA	64.92	52.89	30.81	78.46	72.26	57.24	35.77	80.7
	RES	71.23	64.33	35.61	69.38	74.56	68.07	45.75	73.12
	VEG	76.71	60.79	49.89	87	80.25	67.02	55.01	90.36
	VAC	42.04	43.76	34.61	42.52	36.14	49.54	42.99	48.6
	WAT	96.26	89.25	80.37	93.03	96.59	91.21	82.87	93.44
UA(%)	NRE	51.95	54.1	34.86	68.52	58.93	60.56	41.8	72.1
	POR	86.28	69.73	54.19	/	88.18	71.36	59.82	/
	ROA	70.82	52.57	32.81	75.9	73.42	58.22	38.86	78.63
	RES	63.63	58.17	36.23	63.12	67.76	63.62	42.5	68.77
	VEG	75.8	68.26	44.8	76.94	78.24	71.05	48.01	79.6
	VAC	33.52	48.67	39.26	65.6	46.13	58.81	43.51	71.26
	WAT	97.15	87.62	81.33	95.12	97.31	89.86	85.05	95.17
OA(%)		76.91	65.26	49.04	78.14	79.99	69.66	53.82	80.78

Quantitative accuracy metrics, including overall accuracy (OA), producer's accuracy (PA), and user's accuracy (UA), are utilized to evaluate the FUIS identification performance of SCFN. OA assesses the proportion of correctly classified samples across all categories, providing a general measure of the classification performance. It is computed as the ratio of the sum of correctly classified samples to the total number of reference samples. PA, also known as completeness, refers to the probability that a reference sample in a given class is correctly classified. It is calculated by dividing the number of correctly classified samples in a particular class by the total number of reference samples in that class. UA, also known as reliability, measures the probability that a sample assigned to a specific class truly belongs to that class. UA is determined by computing the ratio of correctly classified samples to the total number of samples predicted to be in a particular class.

The results are presented in Table I. In addition to customized object patch-based inputs and pooling structure, SCFN integrates a fusion structure combining initial scattering features and derived SOCI features. To assess the impact of compactness information, the single scattering object network (SCON) variant of SCFN without compactness information is compared with SCFN. As exhibited in Table I, promising classification performance is achieved by the proposed SCFN model.

On the ALOS-2 fully polarimetric data of HK, SCFN achieved an OA of 79.99%, surpassing the SCON by 3.08%. Similarly, for the ALOS-2 data of Shenzhen, SCFN improved the OA by 2.64% compared with SCON. These results demonstrate the effectiveness of incorporating compactness information for FUIS mapping in different coastal cities. For the GF-3 fully polarimetric data of HK, SCFN attained an OA of 69.66%, outperforming SCON by 4.4%. Even with the dual-polarization ALOS-2 data, SCFN exceeded SCON by 4.78%. The consistent improvements brought by SCFN across various SAR platforms, wavelengths, and polarization settings underscore the robustness and transferability of the proposed method.

The classification accuracy on GF-3 data in HK was lower than that of ALOS-2 fully polarimetric data, possibly due to the lower spatial resolution of GF-3 and its data quality, as evident from Fig. 1, which may have affected the effectiveness of scattering information. On the ALOS-2 dual-polarized data of HK, both methods exhibited relatively lower performance, attributed to the limited polarimetric information provided by only two polarization channels, leading to reduced discriminative power. However, SCFN still surpassed SCON by 4.78% in terms of OA, with varying degrees of improvement in PA and UA. Nevertheless, for the challenging task of FUIS classification in complex urban environments, dual-polarized data are not recommended as effective accuracy may not be achieved.

The results in Shenzhen generally exhibited similar trends to those in HK, validating the effectiveness of the SCFN method in different urban settings. Although the Shenzhen dataset did not include the port category, it still encompassed six main land cover types and the major FUIS classes. The OA differences between the two cities were not substantial. At the category level, water and vegetation were among the most accurately classified

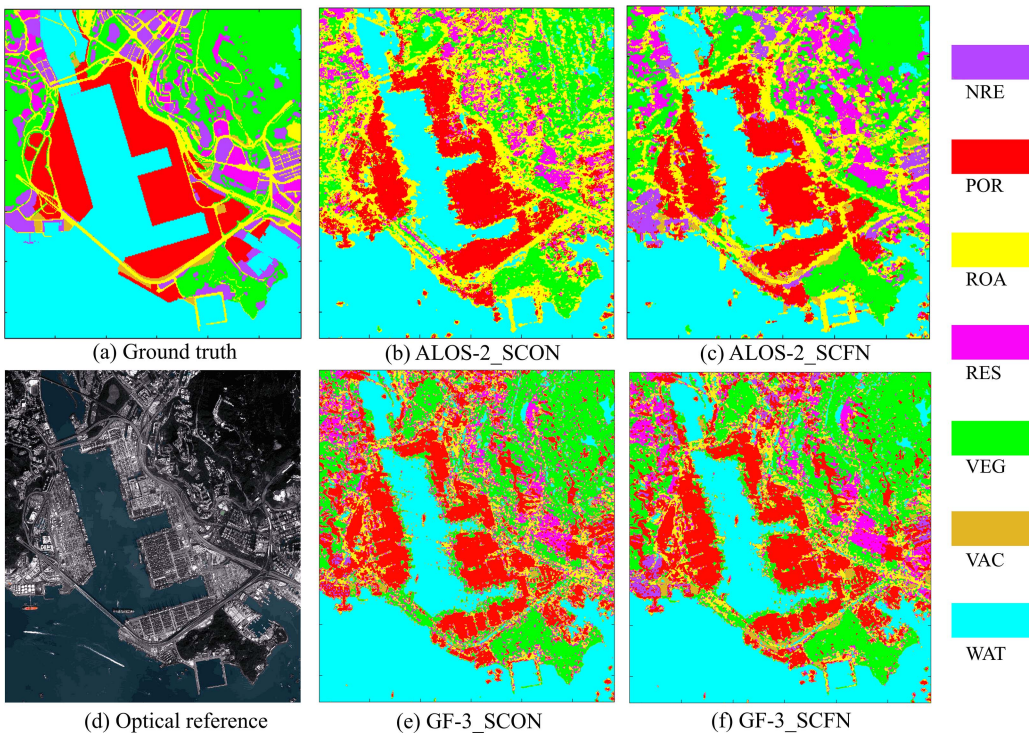

Fig. 6. (a) Labeled ground truth, (d) optical image for reference, and (b) and (c) and (e) and (f) are the classification results of SCON and SCFN from the ALOS-2 and GF-3 data in HK, respectively.

classes in both HK and Shenzhen, owing to their distinct scattering properties in SAR imagery. The accuracies of roads and vacant land were notably higher in Shenzhen compared with HK. This could be explained by the wider roads and more extensive vacant areas in Shenzhen, resulting in less confusion with other land cover types. In both cities, SCFN generally demonstrated higher PA and UA compared with SCON. Incorporating spatial context via the scattering–compactness index in SCFN notably reduced classification confusion between not only the FUIS types but also UIS and NIS, compared with using only polarimetric scattering. Roads and nonresidential buildings showed improved PA and UA exceeding 7%, indicating the value of compactness for differentiating confused impervious surfaces.

Water consistently achieved the highest classification accuracy across all three datasets, owing to its distinctive backscattering characteristics in SAR imagery. The relatively higher accuracy of vegetation in ALOS-2 fully polarimetric data may be attributed to the penetration capability of the *L*-band, providing richer scattering information. In contrast, the *C*-band GF-3 is more sensitive to surface roughness, primarily capturing scattering information from the canopy surface, potentially reducing its sensitivity to internal vegetation features. Vacant land demonstrated notably lower accuracy compared with other categories, likely due to the complex and variable scattering conditions of undeveloped urban surfaces related to moisture, roughness, and ground coverings. Among FUIS classes, ports were most accurately identified due to the dielectric properties of metal containers. Roads, nonresidential buildings, and residential buildings exhibited higher mutual confusion due to similar construction materials and scattering characteristics. Greater confusion existed between FUIS subtypes compared with FUIS and NIS pairs. This is reasonable since functional differences between impervious structures are more subtle to discern from scattering signatures alone.

In summary, SCFN, leveraging joint scattering and compactness, achieved promising FUIS identification results. The proposed SCFN consistently outperformed SCON across different datasets, demonstrating its robustness and generalization ability, and validating the benefits of integrating structural and spatial compactness information for SAR-based urban mapping.

C. FUIS Mapping

To intuitively analyze the classification results, the generated classification maps from the fully polarimetric *L*-band ALOS-2 and *C*-band GF-3 data in HK are presented in Fig. 6. Seven classes are delineated, including port (POR), road (ROA), residential building (RES), nonresidential building (NRE), vegetation (VEG), vacant (VAC), and water (WAT), each denoted by a unique color. Fig. 6(b) and (c) and (e) and (f) illustrates the maps produced by SCON and SCFN from the ALOS-2 and GF-3 data, respectively, while Fig. 6(a) depicts the manual ground truth annotation, and Fig. 6(d) shows the high-resolution WorldView-2 optical image as visual reference.

It can be observed that the complex urban landscape contains intricate networks of roads, mixed distributions of residential and nonresidential buildings. The classification results on the ALOS-2 dataset are generally better than those on GF-3, as shown in Table I. From Fig. 6, we can also notice that the GF-3 results contain more speckle noise, and the road identification

is less precise compared with ALOS-2. However, both datasets achieve relatively consistent and largely accurate classification results.

On both datasets, SCFN achieves promising classification closely matching the reference, with ports mostly successfully extracted, roads reasonably delineated, and a considerable portion of nonresidential structures differentiated from residential houses. However, the inherent scattering similarity poses challenges in separating residential and nonresidential buildings, resulting in confusion. Vacant lands are also largely accurately identified. In vegetated hills, some trees are misclassified as buildings due to mixing, while vegetation is reasonably mapped overall.

In comparison, SCON produces significantly inferior results. It greatly underestimates nonresidential structures by mislabeling them as other FUIS types. Road extraction is less accurate with fragmented outputs, and even some hills are mistaken as roads on ALOS-2. Residential buildings are detected in a fragmented manner, failing to delineate complete structures. Even for the more distinctive ports, SCON misses certain regions, such as the large area on the bottom right on ALOS-2 and overestimates ports on GF-3. Confusions between vegetation and FUIS are more prevalent. Overall, SCON yields more spatially scattered and patchy classification with poorer delineation of integral buildings.

Notably, owing to the time gap between the optical and SAR data, ship locations may differ in the water areas. The ground truth does not label ships. And the small spots on the water in the classification results of SCON and SCFN likely correspond to vessels.

It is also worth noting that the imaging errors inherent to SAR, such as shadow, foreshortening, and layover, do have an impact on the identification of land surfaces, as shown in Fig. 6. For instance, in Fig. 2, which presents the PolSAR scattering images, we can observe the presence of shadows and some foreshortening phenomena in the mountainous areas on the right side on ALOS-2. These imaging issues also exist between the cross-sea bridge and the sea surface. Consequently, as evident in Fig. 6, these factors indeed interfere with the recognition of land surfaces. For example, the vegetation in the mountainous areas might be misclassified as roads or buildings due to these effects. The results indicate that the existing methods still have limitations, and further improvements are necessary to address the imaging issues specific to SAR.

More detailed classification maps from SCON and SCFN are presented in Fig. 7. It can be clearly observed that SCFN achieves noticeably superior identification of FUIS subtypes that are challenging to differentiate based on scattering alone, such as nonresidential versus residential buildings, ports versus roads, and roads versus residential buildings. The compactness information effectively complements the polarimetric scattering to reduce confusion between these impervious surfaces with similar scattering characteristics. In addition, SCFN demonstrates higher accuracy in classifying nonimpervious covers, such as vacant land and vegetation compared with SCON. Moreover, heavy speckle noise can be observed in the SCON maps due to the lack of spatial compactness. In contrast, by incorporating the scattering–compactness index, SCFN exhibits improved spatial continuity and overall outperforms SCON in distinguishing different FUIS and also NIS types from the complex urban environments.

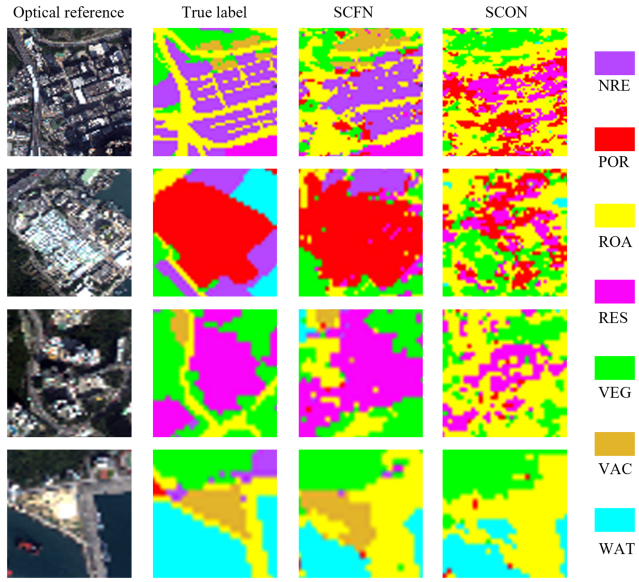

Fig. 7. Detailed classification results of SCON and SCFN.

In summary, the overall classification maps and zoomed subsets highlight the advantages of fusing scattering and compactness cues in SCFN to enhance FUIS identification accuracy. The spatial context aids the classification of impervious surfaces with subtle functional differences and reduces spatially heterogeneous errors. This demonstrates the value of combining polarimetric scattering and scattering–compactness for improved SAR-based urban mapping.

V. Discussion

The proposed SCFN integrates polarimetric scattering features with a novel SOCI for improved FUIS mapping. It introduces key advancements compared with previous studies on PolSAR-based urban mapping. While existing PolSAR-based urban mapping methods primarily rely on pixel-level scattering information [23], [24], [25], our approach introduces an object-based perspective by deriving the SOCI to characterize the spatial compactness properties of urban land covers, providing complementary information to the scattering features. SCFN is tailored to operate on small object-level patches. It demonstrates the effectiveness of using a small 7×7 patch size for classifying impervious surfaces with PolSAR data. The adoption of a smaller patch size is in line with the findings of previous studies in remote sensing image classification [40], [41], [42], [43], [44], [45]. The use of small patch sizes allows for a more focused analysis of the target objects, as smaller patches are more likely to contain homogeneous land cover types. This research advances the understanding of PolSAR scattering mechanisms for FUIS mapping. However, it is important to acknowledge the limitations of SOCI, particularly in handling certain challenging scenarios. For instance, in the case of highly circular impervious

surfaces, SOCI may not always provide optimal performance. Exploring additional contextual information or investigating the use of complementary data sources that can further improve the discrimination of IS and NIS could help to overcome the limitations of SOCI in challenging scenarios.

Experiments validate the proposed method on both *C*-band and *L*-band fully polarimetric data from GF-3 and ALOS-2, as well as dual-polarized data in HK and Shenzhen. Although the two fully polarimetric datasets exhibit differences in accuracy due to variations in wavelength, resolution, and data quality, the effectiveness and applicability of the proposed SOCI and SCFN are demonstrated in both datasets. The method also shows generalizability on dual-polarized data. However, due to the relatively limited information carried by dual-polarized data, it remains challenging to distinguish different urban functional surfaces. There is still room for improvement, particularly in handling challenging scenarios and effectively utilizing dual-polarized data.

In addition, similar to other land use classification studies, the discrimination of certain building types, such as residential and nonresidential buildings, remains challenging due to their similar scattering characteristics [47], [48]. As demonstrated in our results, confusion between these two classes is relatively high. To further improve the separation of these building types, the integration of ancillary data, such as points of interest information, could be explored in future research. Moreover, as reported in other SAR classification studies, the inherent imaging issues of SAR, such as speckle noise, shadow, foreshortening, and layover, can lead to misclassifications [49], [50]. These factors contribute to the uncertainties and errors observed in the classification results. Dedicated techniques for addressing SAR-specific imaging issues could enhance the robustness of the classification results. Furthermore, the complex urban environment poses significant challenges for accurate land cover mapping, particularly in high-density areas with interleaved vegetation and buildings [51]. The presence of occlusions in these regions can hinder the discrimination of different land cover types. Our study also encountered these difficulties, as evident from the confusion between vegetation and buildings in the mountain areas. The incorporation of multiaspect SAR data and the fusion of SAR and optical imagery could potentially alleviate these issues and improve the classification performance in complex urban scenarios.

It is important to acknowledge the limitations of this study. Our intention is to provide a new perspective and method for FUIS mapping in coastal cities and lay the foundation for future applications in other cities. Considering the acquisition cost and processing difficulty of fully PolSAR data, it may not be possible to exhaustively cover all scenarios in a single study. Future research could strive to incorporate more diverse SAR datasets and other urban areas for a more comprehensive analysis.

The improved mapping capability of FUIS using our proposed method has significant implications for urban planning and management. The accurate and detailed representation of urban land cover can help urban planners better understand the spatial distribution of different urban land cover types, guiding informed decision making related to urban development, resource allocation, and environmental management. Moreover, the ability to monitor changes in urban land cover over time enables urban planners to track urban expansion, identify areas of rapid growth, and assess the effectiveness of urban development policies, ensuring sustainable development. Furthermore, detailed FUIS maps can support urban infrastructure planning by providing information on the location and extent of existing impervious surfaces, helping planners identify areas in need of infrastructure upgrades and optimizing the placement of new infrastructure. It also helps urban planners identify areas with high impervious surface coverage, which may be more susceptible to environmental issues, such as urban heat islands, air and water pollution, and stormwater management. This information can inform targeted interventions to mitigate the negative impacts of urbanization on the environment.

VI. Conclusion

This study proposes a scattering–compactness index to extract spatial context information of land surface scattering and develops an SCFN for integrating complementary scattering and compactness cues to enhance FUIS identification in high-density coastal urban environments. Through quantitative and qualitative experiments using *C*-band and *L*-band fully polarimetric GF-3 and ALOS-2 data, as well as dual-polarized SAR data in HK and Shenzhen, the effectiveness and generalizability of the proposed scattering–compactness index and joint scattering–compactness modeling using deep networks are validated. Compared with baselines, over 4% improvement in OA is achieved along with up to 8% increase in PA and UA for detailed FUIS subclass mapping. The proposed algorithm, which exploits the scattering and compactness information derived from SAR data, overcomes limitations in differentiating impervious surfaces with similar scattering responses but distinct spatial contexts, providing a valuable framework for future research on FUIS mapping. Moving forward, further performance gains may be achieved by exploring more advanced SAR imaging techniques and data fusion architectures.

References

[1] B. Neumann, A. T. Vafeidis, J. Zimmermann, and R. J. Nicholls, "Future coastal population growth and exposure to sea-level rise and coastal flooding-a global assessment," *PLoS One*, vol. 10, no. 3, 2015, Art. no. e0118571.

[2] S. Haslett, *Coastal Systems*. Evanston, IL, USA: Routledge, 2008.

[3] A. R. Shahtahmassebi et al., "Remote sensing of impervious surface growth: A framework for quantifying urban expansion and re-densification mechanisms," *Int. J. Appl. Earth Observ. Geoinf.*, vol. 46, pp. 94–112, 2016.

[4] J. Ling, H. S. Zhang, and Y. Y. Lin, "Improving urban land cover classification in cloud-prone areas with polarimetric SAR images," *Remote Sens.*, vol. 13, no. 22, 2021, Art. no. 4708, doi: 10.3390/rs13224708.

[5] M. A. Tanase, M. Santoro, J. de La Riva, F. Perez-Cabello, and T. Le Toan, "Sensitivity of X-, C-, and L-band SAR backscatter to burn severity in Mediterranean pine forests," *IEEE Trans. Geosci. Remote Sens.*, vol. 48, no. 10, pp. 3663–3675, Oct. 2010.

[6] H. Skriver, "Crop classification by multitemporal C- and L-band single- and dual-polarization and fully polarimetric SAR," *IEEE Trans. Geosci. Remote Sens.*, vol. 50, no. 6, pp. 2138–2149, Jun. 2012.

[7] M. Ohki and M. Shimada, "Large-area land use and land cover classification with quad, compact, and dual polarization SAR data by PALSAR-2," *IEEE Trans. Geosci. Remote Sens.*, vol. 56, no. 9, pp. 5550–5557, Sep. 2018.

[8] L. Zhang, S. Zhang, B. Zou, and H. Dong, "Unsupervised deep representation learning and few-shot classification of PolSAR images," *IEEE Trans. Geosci. Remote Sens.*, vol. 60, 2022, Art. no. 5100316.

[9] A. Jamali, S. K. Roy, A. Bhattacharya, and P. Ghamisi, "Local window attention transformer for polarimetric SAR image classification," *IEEE Geosci. Remote Sens. Lett.*, vol. 20, Jan. 2023, Art. no. 4004205.

[10] W. Han, H. Fu, J. Zhu, S. Zhang, Q. Xie, and J. Hu, "A polarimetric projection-based scattering characteristics extraction tool and its application to PolSAR image classification," *ISPRS J. Photogramm. Remote Sens.*, vol. 202, pp. 314–333, 2023.

[11] S. R. Cloude and E. Pottier, "A review of target decomposition theorems in radar polarimetry," *IEEE Trans. Geosci. Remote Sens.*, vol. 34, no. 2, pp. 498–518, Mar. 1996.

[12] R. Touzi, "Target scattering decomposition in terms of roll-invariant target parameters," *IEEE Trans. Geosci. Remote Sens.*, vol. 45, no. 1, pp. 73–84, Jan. 2007.

[13] A. Freeman and S. L. Durden, "A three-component scattering model for polarimetric SAR data," *IEEE Trans. Geosci. Remote Sens.*, vol. 36, no. 3, pp. 963–973, May 1998.

[14] Y. Yamaguchi, T. Moriyama, M. Ishido, and H. Yamada, "Four-component scattering model for polarimetric SAR image decomposition," *IEEE Trans. Geosci. Remote Sens.*, vol. 43, no. 8, pp. 1699–1706, Aug. 2005.

[15] D. L. Evans, T. G. Farr, J. J. van Zyl, and H. A. Zebker, "Radar polarimetry: Analysis tools and applications," *IEEE Trans. Geosci. Remote Sens.*, vol. 26, no. 6, pp. 774–789, Nov. 1988.

[16] J. J. van Zyl, *Synthetic Aperture Radar Polarimetry*. Hoboken, NJ, USA: Wiley, 2011.

[17] M. Jafari, Y. Maghsoudi, and M. J. Valadan Zoej, "A new method for land cover characterization and classification of polarimetric SAR data using polarimetric signatures," *IEEE J. Sel. Topics Appl. Earth Observ. Remote Sens.*, vol. 8, no. 7, pp. 3595–3607, Jul. 2015.

[18] P. Gamba and G. Lisini, "Fast and efficient urban extent extraction using ASAR wide swath mode data," *IEEE J. Sel. Topics Appl. Earth Observ. Remote Sens.*, vol. 6, no. 5, pp. 2184–2195, Oct. 2013.

[19] X. Niu and Y. Ban, "Multi-temporal RADARSAT-2 polarimetric SAR data for urban land-cover classification using an object-based support vector machine and a rule-based approach," *Int. J. Remote Sens.*, vol. 34, no. 1, pp. 1–26, 2013.

[20] Y. Wu, K. Ji, W. Yu, and Y. Su, "Region-based classification of polarimetric SAR images using Wishart MRF," *IEEE Geosci. Remote Sens. Lett.*, vol. 5, no. 4, pp. 668–672, Oct. 2008.

[21] J. Ling and H. Zhang, "WCDL: A weighted cloud dictionary learning method for fusing cloud-contaminated optical and SAR images," *IEEE J. Sel. Topics Appl. Earth Observ. Remote Sens.*, vol. 16, pp. 2931–2941, Mar. 2023.

[22] J. Ling, S. Wei, P. Gamba, R. Liu, and H. Zhang, "Advancing SAR monitoring of urban impervious surface with a new polarimetric scattering mixture analysis approach," *Int. J. Appl. Earth Observ. Geoinf.*, vol. 124, 2023, Art. no. 103541.

[23] G. Sun, J. Cheng, A. Zhang, X. Jia, Y. Yao, and Z. Jiao, "Hierarchical fusion of optical and dual-polarized SAR on impervious surface mapping at city scale," *ISPRS J. Photogramm. Remote Sens.*, vol. 184, pp. 264–278, 2022.

[24] H. Zhang, H. Lin, and Y. Wang, "A new scheme for urban impervious surface classification from SAR images," *ISPRS J. Photogramm. Remote Sens.*, vol. 139, pp. 103–118, 2018.

[25] S. Attarchi, "Extracting impervious surfaces from full polarimetric SAR images in different urban areas," *Int. J. Remote Sens.*, vol. 41, no. 12, pp. 4644–4663, 2020.

[26] L. Wang, P. Marzahn, M. Bernier, and R. Ludwig, "Mapping permafrost landscape features using object-based image classification of multi-temporal SAR images," *ISPRS J. Photogramm. Remote Sens.*, vol. 141, pp. 10–29, 2018.

[27] M. Habibi, M. R. Sahebi, Y. Maghsoudi, and S. Ghayourmanesh, "Classification of polarimetric SAR data based on object-based multiple classifiers for urban land-cover," *J. Indian Soc. Remote Sens.*, vol. 44, pp. 855–863, 2016.

[28] S. Liu, Z. Qi, X. Li, and A. G.-O. Yeh, "Integration of convolutional neural networks and object-based post-classification refinement for land use and land cover mapping with optical and SAR data," *Remote Sens.*, vol. 11, no. 6, 2019, Art. no. 690.

[29] S. Iabchoon, S. Wongsai, and K. Chankon, "Mapping urban impervious surface using object-based image analysis with WorldView-3 satellite imagery," *J. Appl. Remote Sens.*, vol. 11, no. 4, 2017, Art. no. 046015.

[30] L. Zhang, H. Dong, and B. Zou, "Efficiently utilizing complex-valued PolSAR image data via a multi-task deep learning framework," *ISPRS J. Photogramm. Remote Sens.*, vol. 157, pp. 59–72, 2019, doi: 10.1016/j.isprsjprs.2019.09.002.

[31] Z. Shao, T. Cheng, H. Fu, D. Li, and X. Huang, "Emerging issues in mapping urban impervious surfaces using high-resolution remote sensing images," *Remote Sens.*, vol. 15, no. 10, 2023, Art. no. 2562.

[32] N. Hoang, "Automatic impervious surface area detection using image texture analysis and neural computing models with advanced optimizers," *Comput. Intell. Neurosci.*, vol. 2021, 2021, Art. no. 8820116.

[33] X. Dong, Z. Meng, Y. Wang, Y. Zhang, H. Sun, and Q. Wang, "Monitoring spatiotemporal changes of impervious surfaces in Beijing City using random forest algorithm and textural features," *Remote Sens.*, vol. 13, no. 1, 2021, Art. no. 153.

[34] S. R. Cloude and E. Pottier, "An entropy based classification scheme for land applications of polarimetric SAR," *IEEE Trans. Geosci. Remote Sens.*, vol. 35, no. 1, pp. 68–78, Jan. 1997.

[35] H. Zhang, H. Lin, Y. Li, Y. Zhang, and C. Fang, "Mapping urban impervious surface with dual-polarimetric SAR data: An improved method," *Landscape Urban Plan.*, vol. 151, pp. 55–63, 2016, doi: 10.1016/j.landurbplan.2016.03.009.

[36] H. Sui, K. An, C. Xu, J. Liu, and W. Feng, "Flood detection in PolSAR images based on level set method considering prior geoinformation," *IEEE Geosci. Remote Sens. Lett.*, vol. 15, no. 5, pp. 699–703, May 2018.

[37] L. Yang, X. Feng, F. Liu, J. Liu, and X. Sun, "Potential of soil moisture estimation using C-band polarimetric SAR data in arid regions," *Int. J. Remote Sens.*, vol. 40, no. 5/6, pp. 2138–2150, 2019.

[38] L. Brodský and L. Borůvka, "Object-oriented fuzzy analysis of remote sensing data for bare soil brightness mapping," *Soil Water Res.*, vol. 1, no. 3, pp. 79–84, 2006.

[39] M. Tan and Q. V. Le, "EfficientNet: Rethinking model scaling for convolutional neural networks," in *Proc. 36th Int. Conf. Mach. Learn.*, 2019, pp. 6105–6114.

[40] Q. Gao, S. Lim, and X. Jia, "Hyperspectral image classification using convolutional neural networks and multiple feature learning," *Remote Sens.*, vol. 10, no. 2, 2018, Art. no. 299.

[41] X. Zhang, S. Shang, X. Tang, J. Feng, and L. Jiao, "Spectral partitioning residual network with spatial attention mechanism for hyperspectral image classification," *IEEE Trans. Geosci. Remote Sens.*, vol. 60, 2022, Art. no. 5507714.

[42] A. Sharma, X. Liu, X. Yang, and D. Shi, "A patch-based convolutional neural network for remote sensing image classification," *Neural Netw.*, vol. 95, pp. 19–28, 2017.

[43] S. Park and N.-W. Park, "Effects of class purity of training patch on classification performance of crop classification with convolutional neural network," *Appl. Sci.*, vol. 10, no. 11, 2020, Art. no. 3773.

[44] H. Zhang, L. Wan, T. Wang, Y. Lin, H. Lin, and Z. Zheng, "Impervious surface estimation from optical and polarimetric SAR data using small-patched deep convolutional networks: A comparative study," *IEEE J. Sel. Topics Appl. Earth Observ. Remote Sens.*, vol. 12, no. 7, pp. 2374–2387, Jul. 2019.

[45] L. Wan, H. Zhang, G. Lin, and H. Lin, "A small-patched convolutional neural network for mangrove mapping at species level using high-resolution remote-sensing image," *Ann. GIS*, vol. 25, no. 1, pp. 45–55, 2019.

[46] M. Dabboor, S. Howell, M. Shokr, and J. Yackel, "The Jeffries–Matusita distance for the case of complex Wishart distribution as a separability criterion for fully polarimetric SAR data," *Int. J. Remote Sens.*, vol. 35, no. 19, pp. 6859–6873, 2014.

[47] D. Xiang, T. Tang, Y. Ban, Y. Su, and G. Kuang, "Unsupervised polarimetric SAR urban area classification based on model-based decomposition with cross scattering," *ISPRS J. Photogramm. Remote Sens.*, vol. 116, pp. 86–100, 2016.

[48] R. Jaturapitpornchai, M. Matsuoka, N. Kanemoto, S. Kuzuoka, R. Ito, and R. Nakamura, "Newly built construction detection in SAR images using deep learning," *Remote Sens.*, vol. 11, no. 12, 2019, Art. no. 1444.

[49] P. Wang, H. Zhang, and V. M. Patel, "SAR image despeckling using a convolutional neural network," *IEEE Signal Process. Lett.*, vol. 24, no. 12, pp. 1763–1767, Dec. 2017.
[50] H. Zhu, R. Leung, and M. Hong, "Shadow compensation for synthetic aperture radar target classification by dual parallel generative adversarial network," *IEEE Sensors Lett.*, vol. 4, no. 8, Aug. 2020, Art. no. 7002904.
[51] P. Gamba, M. Aldrighi, and M. Stasolla, "Robust extraction of urban area extents in HR and VHR SAR images," *IEEE J. Sel. Topics Appl. Earth Observ. Remote Sens.*, vol. 4, no. 1, pp. 27–34, Mar. 2011.

Jing Ling (Graduate Student Member, IEEE) received the B.Eng. degree in remote sensing science and technology and the M.Sc. degree in cartography and geography information system from the School of Remote Sensing and Information Engineering, Wuhan University, Wuhan, China, in 2017 and 2020, respectively. She is currently working toward the Ph.D. degree in remote sensing with the Department of Geography, The University of Hong Kong, Hong Kong, China.

Her research interests include urban remote sensing and multisource data fusion.

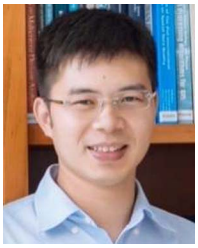

Hongsheng Zhang (Senior Member, IEEE) received the B.Eng. degree in computer science and technology and the M.Eng. degree in computer applications technology from South China Normal University, Guangzhou, China, in 2007 and 2010, respectively, and the Ph.D. degree in Earth system and geoinformation science from The Chinese University of Hong Kong, Hong Kong, in 2013.

He is currently an Assistant Professor with the Department of Geography, The University of Hong Kong, Hong Kong. His research interests include remote-sensing applications in tropical and subtropical areas, with a focus on the urban environment and coastal sustainability monitoring, using multisource remote sensing data fusion and image pattern recognition techniques.

Rui Liu (Graduate Student Member, IEEE) received the B.Eng. degree in remote sensing information engineering and the M.Eng. degree in intelligent system and pattern recognition from the School of Remote Sensing and Information Engineering, Wuhan University, Wuhan, China, in 2018 and 2021, respectively. He is currently pursuing the Ph.D. degree in remote sensing with the Department of Geography, The University of Hong Kong, Hong Kong, China.

His research interests include multimodal data processing, deep learning technology, and knowledge transfer.

Yinyi Lin (Member, IEEE) received the B.Eng. degree in geographical conditions monitoring from the School of Remote Sensing and Information Engineering, Wuhan University, Wuhan, China, in 2017, and the Ph.D. degree in Earth system and geoinformation science from The Chinese University of Hong Kong, Hong Kong, in 2021.

She is currently a Postdoctoral Fellow with the Department of Geography, The University of Hong Kong, Hong Kong. Her research interests include multisource data fusion and urban remote sensing.